A Coupling-Adaptive Wireless Power Transfer System with Voltage-/Current-Mode Receiver and Global Digital-PWM Regulation

Lu, Tianqi; Du, Sijun

DOI
10.1109/JSSC.2024.3461857

Publication date
2024

Document Version
Final published version

Published in
IEEE Journal of Solid-State Circuits

A Coupling-Adaptive Wireless Power Transfer System With Voltage-/Current-Mode Receiver and Global Digital-PWM Regulation

Tianqi Lu, *Graduate Student Member, IEEE*, and Sijun Du, *Senior Member, IEEE*

***Abstract*— This article presents a 13.56-MHz wireless power transfer (WPT) system with coupling variation robustness and high efficiency for powering biomedical implantable devices (IMDs). To sustain reliable power transfer against inductive-link fluctuation, a hybrid voltage-/current-mode (V/CM) receiver (RX) is proposed to provide CM recovery when the coupling becomes weak for VM operation. To optimize the end-to-end (E2E) efficiency, a digital pulsewidth modulation (PWM)-based global power regulation technique is proposed, which allows a fully on/off operation of the three-mode power amplifier (PA) at the transmitter (TX) side and fast load-transient responses. Moreover, the system adopts a fully integrated voltage-sensing load-shift-keying (LSK) demodulation technique, which replaces conventional current sensing methods with a streamlined implementation and reduced power consumption. Both prototype TX and RX chips were fabricated in a 180-nm CMOS process. The proposed system, powered by a 1.8-V supply at TX, realizes a regulated 1.8-V dc output at RX. With the help of the hybrid V/CM RX, the proposed system achieves an up-to-150% WPT range extension compared to VM-only operation and an up to 7.2-cm WPT range. Benefiting from the global digital-PWM regulation, it achieves up to 72.3% E2E efficiency over the loading range from 0.18 to 81 mW. A 10-μs load-transient recovery is also attained at a 164× load step with a 110-mV undershoot and unnoticeable overshoots.**

***Index Terms*— Coupling adaptive, global digital-pulsewidth modulation (PWM) regulation, voltage-/current-mode (V/CM) receiver (RX), voltage-sensing load-shift-keying (LSK) demodulation, wireless power transfer (WPT).**

I. Introduction

WIRELESS power transfer (WPT) is a promising technology for powering biomedical implantable devices (IMDs), such as neural stimulators, retinal prostheses, and brain interfaces [1]. In such applications, a WPT system typically faces a varying coupling condition in the inductive link. For instance, in a retinal prosthesis system, the transmitter (TX) coil and the receiver (RX) coil often show misalignment due to the relative movement between eyeballs and glasses [2]. To ensure proper operations of IMDs, the WPT system should reliably deliver power across the link against the varying coupling conditions. On the other hand, the WPT system shows a primary requirement for high power efficiency, at both the RX and system levels. On the RX side, local overheating can result in severe medical issues, which should be avoided by high power conversion efficiency (PCE). At the system end-to-end (E2E) level (from TX to RX), reduced power loss extends the overall WPT system's lifespan, which is typically battery-powered for portability, and also alleviates the aging effect of power components. Furthermore, a biomedical WPT system should have a high integration level for both cost and size considerations. Achieving high efficiency and robustness against coupling variations should not sacrifice the power density and practicality.

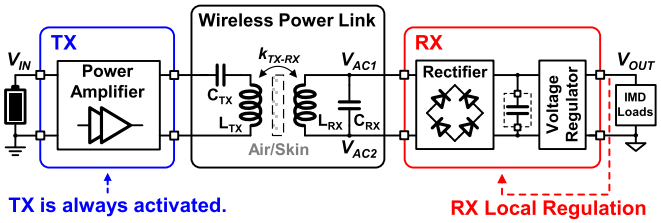

Fig. 1. Conventional WPT system for biomedical IMD.

Fig. 1 shows a conventional WPT system for IMD applications. The wireless power is emitted from an always-activated power amplifier (PA) at TX and received by a two-stage RX, including an open-loop rectifier stage and a voltage regulator [3], [4], [5], [6]. Typically, the rectifier stage is a voltage-mode (VM) full-bridge rectifier (FBR) or a voltage doubler (VD), while the voltage regulator is simply a low-drop regulator or a switched dc–dc converter. Due to the always-on power emission from TX, the E2E efficiency is low, especially when the IMD loading is light. Moreover, the two-stage structure of RX shows cascaded power losses and high system cost and volume.

To address the abovementioned issues, WPT systems with single-stage RX and global power control have been recently reported. Li et al. [7] introduced a WPT system with a single-stage 1X/2X regulating rectifier at RX and global power control assisted by a supply modulator at TX. It improves E2E efficiency to 62.4% with, however, many external components at TX, including a bulky sensing coil and an off-chip global controller. The sensing coil is used to perform resonant current sensing to achieve load-shift-keying (LSK) signal demodulation for in-band RX-to-TX data transfer, while the off-chip

Received 13 May 2024; revised 8 July 2024 and 6 September 2024; accepted 8 September 2024. Date of publication 25 September 2024; date of current version 25 November 2024. This article was approved by Associate Editor Yan Lu. *(Corresponding author: Sijun Du.)*

The authors are with the Department of Microelectronics, Delft University of Technology, 2628 CD Delft, The Netherlands (e-mail: sijun.du@tudelft.nl).

Color versions of one or more figures in this article are available at https://doi.org/10.1109/JSSC.2024.3461857.

Digital Object Identifier 10.1109/JSSC.2024.3461857

global controller involves data receivers (RXs), decoders, digital-to-analog converters (DACs), and so on. Besides, the supply modulator at TX introduces cascaded power losses with extra power components. To further save power and components, both single-stage TX and RX topologies have been realized in prior works such as [8], [9], and [10], with global power control. The simplified power stages in these works contribute to higher peak E2E efficiency, that is, 70.6% in [8], 71.5% in [9], and 70.1% in [10]. Nonetheless, these works still require a bulky sensing coil at TX for RX-to-TX data transfer. To further improve the integration level of WPT systems, fully integrated global power control methods have been presented [11], [12]. In [11], an on-chip current sensor replaces the conventional sensing coil. Though the sensor solution reduces the packaging complexity and cost at TX, its current-mirror topology imposes a high power budget due to the large variations in the TX current amplitude. A phase shift-keying method was proposed in [12] without a sensing coil; however, it is only valid for a series-to-series resonant wireless link, which is not suitable for low-power IMDs [13].

Among prior WPT system designs, most works mainly focus on enhancing the E2E efficiency by both simplifying the power stage and enabling global power control. In addition, in-band wireless data transfer has emerged as a viable solution to eliminate bulky and costly off-chip components. However, existing literature predominantly addresses performances solely in strong-coupling conditions, while the link coupling can vary largely and unpredictably in biomedical applications. Given the absence of system-level weak-coupling techniques, the variable link remains an unexplored concern necessitating immediate attention.

In this article [14], a 13.56-MHz coupling-adaptive WPT system is proposed with a single-stage RX, a single-stage TX, and fully integrated global power control. At RX, the variable link coupling is addressed through a hybrid V-/current-mode (V/CM) rectifier, which performs CM recovery when the inductive link coupling is too weak to sustain VM operation. At TX, a three-mode class-D PA is adopted with digital pulsewidth modulation (PWM)-based global power control, optimizing the tradeoff between output power and E2E efficiency. Moreover, a voltage-sensing LSK demodulation method is proposed to replace the current sensing methods, simplifying the demodulator implementation and saving power. The remainder of the article is organized as follows. Section II presents the topology of the proposed coupling-adaptive WPT system. Section III shows the system schematic and circuit implementations. Experimental results and conclusions are given in Sections IV and V, respectively.

II. Proposed Coupling-Adaptive WPT System

Fig. 2 presents the power stage of the proposed coupling-adaptive WPT system, which comprises three stages: RX, TX, and wireless link. The RX is based on a full-wave VD topology involving M_P, M_N, C_{O1}, and C_{O2}. The switch S_{LC} is serially connected with C_{RX}, facilitating resonant CM operation. The switch S_{LSK} enables LSK modulation by short-circuiting L_{RX}, achieving RX-to-TX data transfer. The detailed operation of RX will be presented in Section II-A. The TX

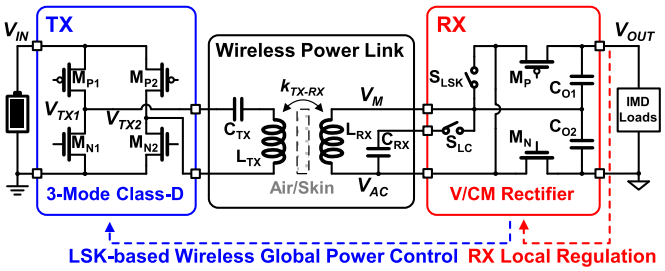

Fig. 2. Proposed coupling-adaptive WPT system topology.

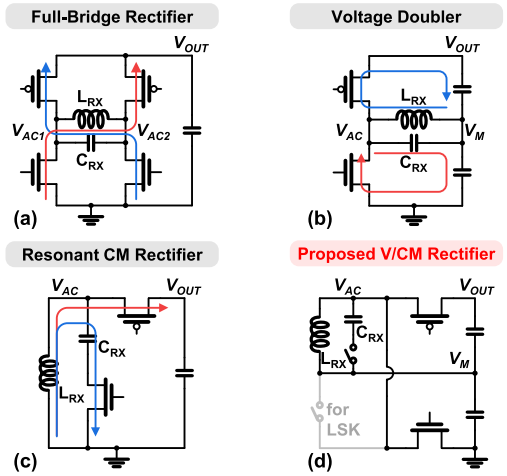

Fig. 3. Single-stage RX topologies. (a) FBR. (b) VD. (c) Resonant CM rectifier. (d) Proposed V/CM rectifier.

adopts a full-bridge class-D PA, consisting of four power transistors, M_{P1}, M_{P2}, M_{N1}, and M_{N2}. It enables a three-mode operation with three output power levels, which will be detailed in Section II-B. The wireless link incorporates a series-resonance L_{TX}–C_{TX} tank at TX and a parallel-resonance L_{RX}–C_{RX} tank at RX, ensuring both high power and high efficiency across the link [13].

A. Hybrid V/CM RX

Interfacing the wireless link, RX is uppermost in a WPT system. With strongly coupled link conditions, single-stage VM rectifiers are widely adopted, such as FBR [11], [15], [16], [17], [18], [19] and VD [20], [21], [22], as shown in Fig. 3(a) and (b), respectively. They can attain high PCE and high output power, benefiting from the simplified power paths and the VM principle. However, their voltage conversion ratio (VCR) is limited to 1 and 2 for FBR and VD, respectively. Unlike a two-stage RX that can compensate for the VCR by a cascaded dc–dc converter, low-VCR single-stage RXs cannot maintain operation when the input power becomes low. To handle the weak input at RX, a resonant CM rectifier was introduced [23], as shown in Fig. 3(c). With the help of a resonance phase, the CM rectifier can build up the energy in the L_{RX}–C_{RX} tank in a few periods, thus overcoming the VCR limitation in VM topologies. Nonetheless, the resonance phase brings over-voltage risks if the input power becomes high, limiting its effectiveness in strong-coupling conditions [24].

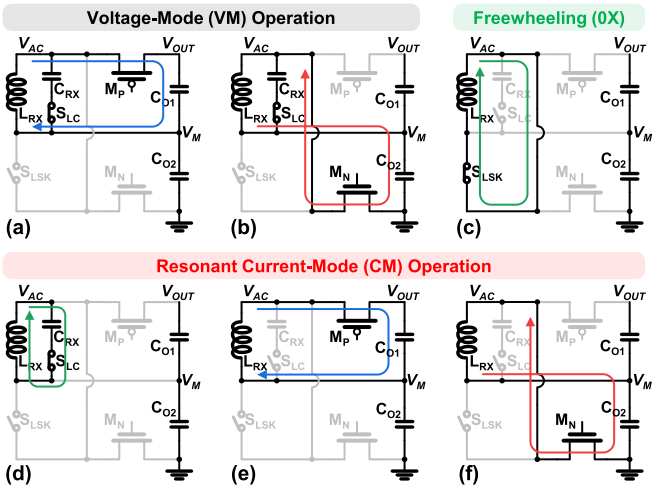

Fig. 4. Operation principle of the proposed V/CM RX. (a) VM C_{O1}-charging phase. (b) VM C_{O2}-charging phase. (c) Freewheeling (0X) phase. (d) CM resonance phase. (e) CM C_{O1}-charging phase. (f) CM C_{O2}-charging phase.

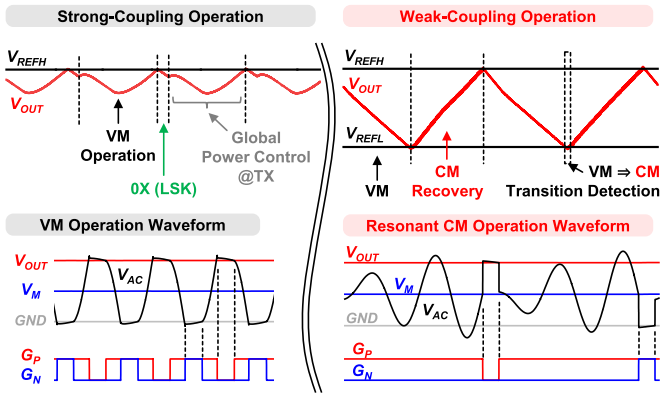

Fig. 5. Operation waveform of the proposed V/CM RX.

A VM/CM reconfigurable rectifier was presented in [25] and [26], employing a VM half-bridge rectifier (HBR) with a CM passive diode path. Though it exposed the gap between VM and CM rectifiers, the approach of simply combining two operation modes did not fully address the mode transition challenges by missing effective input power detection. The passive diode operation resulted in PCE below 77%. In addition, the used HBR topology may pose challenges for low-power IMDs due to the over-voltage risk at the ac input node.

To address the abovementioned issues and constructively fill the gap between VM and CM rectifiers, this work proposes a hybrid V/CM rectifier with active full-wave operation and seamless mode transition, as shown in Fig. 3(d). It employs three power switches, M_P, M_N, and S_{LC}, one LSK switch, S_{LSK}, and two output capacitors, C_{O1} and C_{O2}. It has six operation phases, as shown in Fig. 4. The detailed operation is explained in the following.

1) *VM Operation*: In strong-coupling conditions, the proposed RX works in VM as a full-wave VD. It has two VM phases. When the input voltage of RX, V_{AC}, is higher than the output voltage of RX, V_{OUT}, it turns on M_P to enter the C_{O1}-charging phase, as shown in Fig. 4(a). As V_{AC} is lower than ground, it switches to the C_{O2}-charging phase by turning on M_N, as shown in Fig. 4(b). During the VM operation, S_{LC} is always turned on to form a parallel L_{RX}–C_{RX} resonance tank.
2) *Freewheeling (0X) Operation*: To generate LSK signal for global power control and regulate V_{OUT}, the proposed RX enters the freewheeling (0X) phase periodically. In 0X phase, S_{LSK} is turned on to short-circuit L_{RX}, and M_P, M_N, and S_{LC} are all turned off, as shown in Fig. 4(c).
3) *Resonant CM Operation*: In weak-coupling conditions, the proposed RX works as a resonant CM rectifier with three CM phases. Fig. 4(d) shows the resonance phase, during which only S_{LC} is turned on, allowing resonance energy to accumulate in the L_{RX}–C_{RX} tank. Once the accumulated energy reaches a sufficient level, the RX enters either the C_{O1}-charging phase or the C_{O2}-charging phase, as depicted in Fig. 4(e) and (f), respectively. The CM charging phases are triggered only when V_{AC} equals V_M so that the entire resonance energy is stored in L_{RX}. During the CM charging phases, L_{RX} performs as a current source, and C_{RX} is disconnected from the circuit.

Fig. 5 shows the operation waveform of the proposed RX. In strong-coupling conditions, it simply works in VM. Upon V_{OUT} surpassing the upper threshold voltage, V_{REFH}, it enters 0X phase for 0.6 μs, generating an LSK signal that triggers global power control at TX to achieve output regulation. In case the link coupling weakens, V_{OUT} decreases due to insufficient input power at RX. When V_{OUT} falls below the lower threshold voltage, V_{REFL}, a VM-to-CM transition detection will be initiated. The proposed RX will seamlessly switch to CM operation to recover V_{OUT} if it is identified as weak coupling. The coupling identification process will be detailed in Section III-A. Given that the wireless link can revert to strong coupling at any moment and the VM operation offers advantages such as high PCE, the proposed RX automatically backs to VM operation when V_{OUT} is recovered to V_{REFH}, eliminating the need for the CM-to-VM transition detection.

B. Three-Mode TX

In WPT applications, the PA at TX is typically realized using a class-D or a class-E topology to achieve high efficiency. While a class-E PA has the potential to achieve higher power efficiency at high frequencies by employing a single power switch, it encounters challenges in handling high voltage swings and addressing impedance mismatching [27], [28]. Therefore, this work adopts a class-D PA for both high efficiency and high reliability. As shown in Fig. 6, the adopted class-D PA has a full bridge topology, comprising four power transistors, M_{P1}, M_{P2}, M_{N1}, and M_{N2}, and three operation modes. The detailed operation is explained in the following.

1) *Full-Bridge (2X) Mode*: The class-D PA works as a full bridge by activating all four power transistors to attain high output power. The two phases in the 2X mode are shown in Fig. 6(a) and (b). The switching node swing, $V_{TX1} - V_{TX2}$, equals $2V_{IN}$.

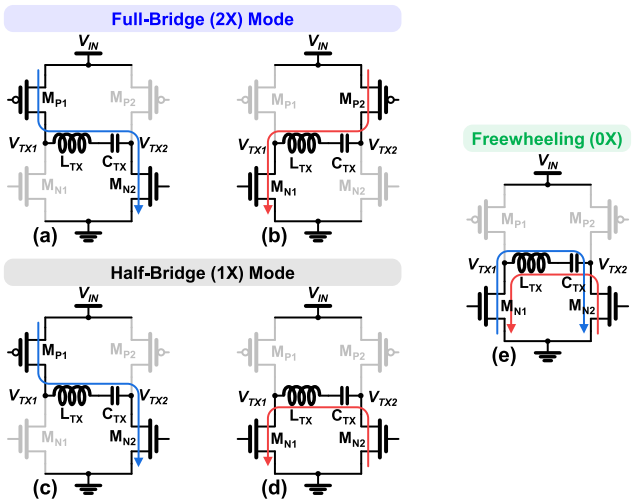

Fig. 6. Operation principle of the three-mode TX. (a) and (b) Full-bridge (2X) operation mode. (c) and (d) Half-bridge (1X) operation mode. (e) Freewheeling (0X) mode.

2) *Half-Bridge (1X) Mode*: The class-D PA works as a half-bridge by only activating M_{P1} and M_{N1}, while M_{P2} keeps off and M_{N2} keeps on. Fig. 6(c) and (d) shows the two phases in the 1X mode. Given that V_{TX2} is tied to ground, the swing of $V_{TX1} - V_{TX2}$ is only V_{IN}.
3) *Freewheeling (0X) Mode*: By turning on both M_{N1} and M_{N2} while turning off both M_{P1} and M_{P2}, the class-D PA is freewheeling with the residual energy in the L_{TX}–C_{TX} tank. In the 0X mode, no power is drained from V_{IN}, and the swing of $V_{TX1} - V_{TX2}$ becomes near zero.

To achieve global power control, the TX alternates the operation between an active (2X or 1X) mode and the 0X mode. In the 2X mode, the TX emits 4× power of the 1X mode [9], [29], thus enhancing its heavy-load or weak-coupling performance. In contrast, the 1X-mode TX shows higher power efficiency by saving switching losses and reducing loop current, which also results in a smaller V_{OUT} ripple. Therefore, the tradeoff between the output power and the power efficiency is optimized at TX by properly selecting the active mode, which will be further detailed in Section III-B.

C. Global PWM Regulation

Global power control should be tailored to meet the needs of various biomedical applications. Continuous control methods, such as supply modulation, are preferred for high-power (>1 W) applications [7], [9], [30], while discontinuous control methods are widely applied in sub-100-mW low-power applications. In [8], a global constant-idle-time control was reported, which deactivates the TX power stage for a certain period upon the RX output voltage exceeding a threshold. Though this non-linear approach shows a stable loop and fast transient responses, it faces large voltage ripples in heavy-load conditions and limited light-load E2E efficiency. To address this, a global hysteretic control method was reported in [11], as shown in Fig. 7(a). It improves light-load efficiency by incorporating longer idle periods; however, it necessitates additional power consumption at TX for LSK demodulation

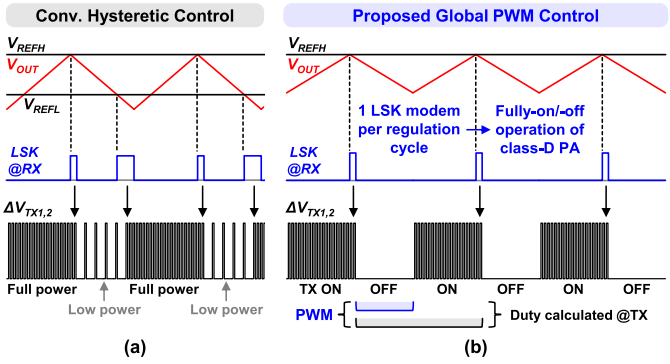

Fig. 7. (a) Conventional hysteretic control [11]. (b) Proposed global PWM control.

during the low-power mode. Furthermore, the low-power mode restricts the adjustable power range, thereby limiting its efficacy in accommodating varying coupling conditions [31].

Fig. 7(b) depicts the proposed global PWM control. It adjusts the on/off duty ratio of the TX power stage based on monitoring the PWM period. If the PWM period exceeds the predetermined reference duration, the TX will decrease the off time, and vice versa. Therefore, the heavy (or light) load condition corresponds to a short (or long) off period. Compared to the constant-idle-time control, the proposed PWM control achieves a better tradeoff between power efficiency and output ripple. Compared to the hysteretic control, it only requires one LSK modem in each regulation cycle, allowing the TX power stage to have a reliable fully on/off operation without extra LSK-demanded power dissipation.

III. System and Circuit Implementations

Fig. 8 shows the overall architecture of the proposed 13.56-MHz coupling-adaptive WPT system with in-band uplink data transfer. On the RX chip, S_{LC} and S_{LSK} are implemented by transmission gates. The three power switches, M_P, M_N, and S_{LC}, are sized differently for VM and CM operations with distinct power levels. The VM size of S_{LC} is designed to be considerably large to minimize the conduction loss, given its infrequent switching. The output voltage, V_{OUT}, is monitored by the output detector, which generates a regulation signal V_{REG} directly controlling S_{LSK} and a mode-transition detection trigger signal V_{MDDET}. Enabled by V_{MDDET}, the mode-transition detector performs open-circuit V_{AC} detection to commence mode transition between VM and CM. The switching controller determines the accurate turn-on/-off moments of M_P and M_N using an adaptive delay compensation technique. The gate driving controller at RX finalizes the gate voltages V_{GSLC}, V_{GP}, and V_{GN}. On the TX chip, the gate driving signals for the class-D PA have been designed with dead time to avoid short circuits between V_{IN} and ground [10]. The global digital-PWM controller generates a regulation signal V_{DUTY}, reflecting the on/off duty ratio of TX, and chooses an active mode between 1X and 2X modes. The voltage-sensing LSK demodulator interfaces a divided voltage swing on C_{TX}, using an on-chip capacitive divider, and sends the demodulated data, V_{LSK}, to the global digital-PWM controller.

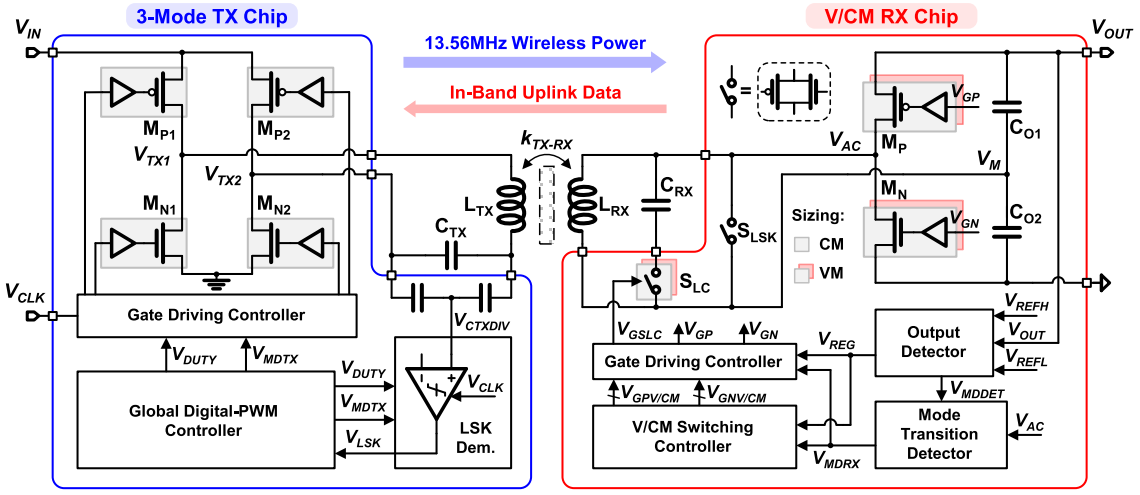

Fig. 8. Overall architecture of the proposed coupling-adaptive WPT system.

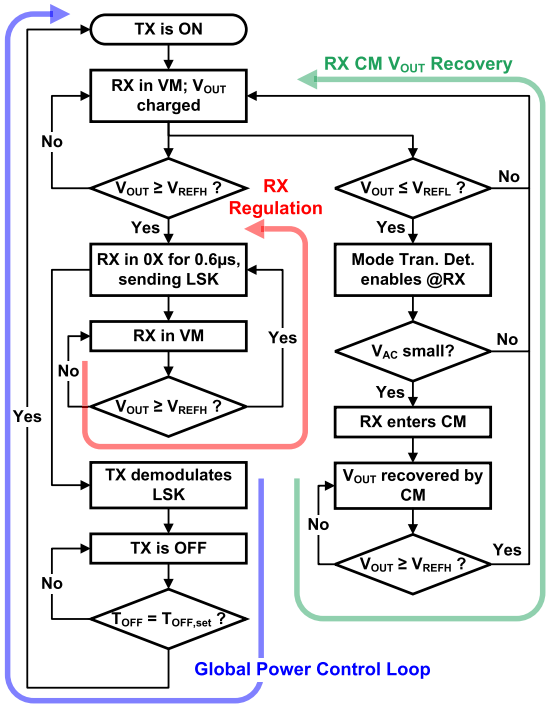

Fig. 9. Operation flowchart of the proposed coupling-adaptive WPT system.

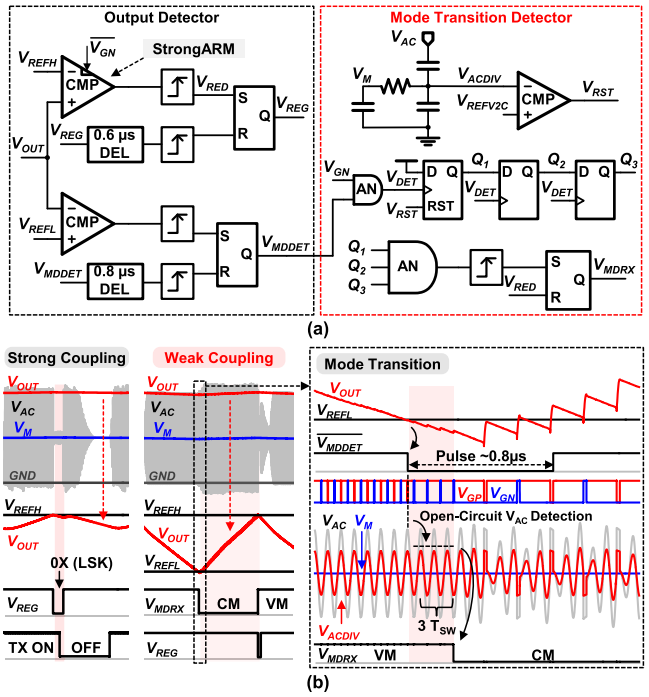

Fig. 10. Output detector and mode transition detector at RX. (a) Implementation. (b) Operation waveform.

Fig. 9 summarizes the operation flow of the proposed WPT system. It involves three main control loops: the global power control loop, the RX local V_{OUT} regulation loop, and the RX CM V_{OUT} recovery loop. The involvement of the loops depends on the coupling and loading conditions, which will be elucidated shortly.

A. Hybrid V/CM RX Implementation

Fig. 10 shows the output detector and the mode transition detector at RX. V_{OUT} is compared to V_{REFH} using a StrongARM comparator clocked by inverted V_{GN}. Once V_{OUT} exceeds V_{REFH}, V_{REG} will present a 0.6-μs pulse, switching RX to 0X phase. If V_{OUT} continuously exceeds V_{REFH} after the 0X pulse, another 0X pulse will be immediately generated. The multi-pulse LSK signal can result in a more pronounced impedance change reflected at TX, enhancing the robustness of data transfer. Moreover, it inherently operates as constant-off-time control, serving as the RX local V_{OUT} regulation method, as will be demonstrated in the measurement section.

As shown in Fig. 10, V_{MDDET} can generate a 0.8-μs pulse when V_{OUT} falls below V_{REFL}, initiating the mode transition detection. Instead of immediately switching to CM, an additional verification step is introduced to mitigate false triggers caused by unpredictable V_{OUT} undershoots. During the pulse, M_P is turned off, while M_N continues to operate as an active diode. This scenario indicates that the RX alternates between the resonance phase and the VM C_{O2}-charging phase, as depicted in Fig. 4(d) and (b), respectively. In this configuration, the open-circuit V_{AC} can be detected because the L_{RX}–C_{RX} tank is able to resonate freely during

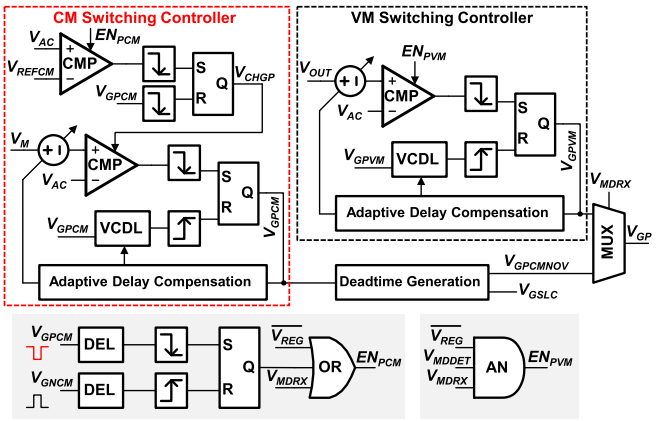

Fig. 11. Switching controller of M_P at RX.

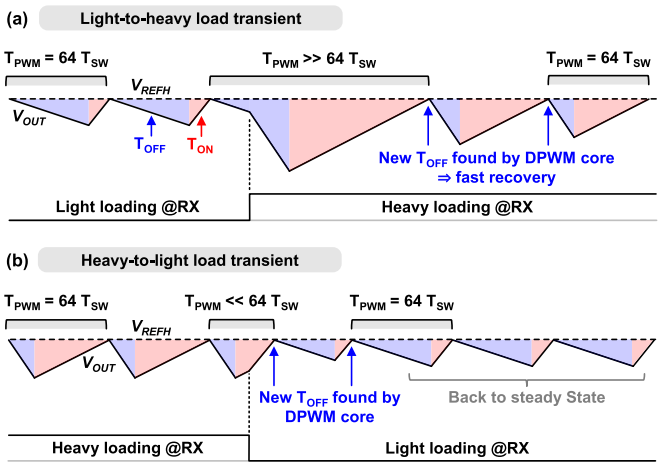

Fig. 12. Operation principle of the proposed digital-PWM control. (a) Light-to-heavy load transient. (b) Heavy-to-light load transient.

positive half cycles without being clamped by V_{OUT}. For reliable VM-to-CM transition, the divided version of V_{AC}, V_{ACDIV}, must remain below the threshold voltage V_{REFV2C} for three consecutive switching periods (T_{SW}) to reflect the weak-coupling condition. The CM-to-VM transition happens automatically upon V_{OUT} touching the upper boundary V_{REFH}.

Fig. 11 shows the switching controller of M_P. Operating at 13.56 MHz, even a small control loop delay can result in significant switching errors in the power path [32], [33]. Therefore, a fast-responding adaptive delay compensation technique is adopted [22]. In the VM switching controller, the M_P turn-on moment is determined by a comparator with a delay-compensating input offset; the M_P turn-off moment is governed by a voltage-controlled delay line (VCDL). In the CM switching controller, the timing determination mechanism is similar to the VM loop, while an additional energy detector is added to monitor V_{AC} during the CM resonance phase. The CM switching controller generates gate signals for both M_P and S_{LC}. To prevent a short circuit from V_{OUT} to RX ground during the switching moment of both switches, a dead time is designed to slightly lag $V_{GPCMNOV}$ behind V_{GSLC}. A multiplexer selects V_{GP} from V_{GPVM} or $V_{GPCMNOV}$ based on V_{MDRX}. Thanks to the adaptive delay compensation, the complex control loop does not introduce additional power loss in the power path. The switching controller of M_N is implemented similarly, while M_P and M_N are enabled alternately for a balanced energy distribution between C_{O1} and C_{O2}.

B. Global Digital-PWM Controller

Using the global PWM control in WPT scenarios, the reference PWM duration should be selected to optimize the tradeoff between E2E efficiency and V_{OUT} ripple. A shorter PWM period helps achieve a smaller V_{OUT} ripple; however, this implies more frequent turn-on/-off of the PA at TX. In practice, the resonant wireless link requires start-up phases to build energy before commencing power transfer; moreover, considerable residual energy can remain in the L_{TX}–C_{TX} tank after turning off the PA, only a small portion of which can be further transferred to RX. Thus, frequent turn-on/-off of the PA at TX often results in limited TX power efficiency and, thus, degraded E2E efficiency [11]. In this work, the reference PWM duration is set to 64 × T_{SW}, given the above tradeoff.

Typically, a PWM control can be realized by comparing a sawtooth wave to a dc reference voltage, with frequency compensation ensuring loop stability. However, it suffers from slow load-transient responses and long settling times, resulting in large voltage ripple during light-to-heavy load transients and degraded E2E efficiency after heavy-to-light load transients [10]. To solve this, a digital PWM algorithm is proposed in this work, whose operation principle is shown in Fig. 12. When one PWM period (T_{PWM}) ends by demodulating the LSK signal from RX, the TX directly calculates the next off time (T_{OFF}) based on the T_{PWM} and the last T_{OFF}. The relation can be expressed as follows:

$$\frac{T_{OFF}}{T_{PWM}} = \frac{T_{OFF,next}}{T_{PWM,set}} \tag{1}$$

where $T_{PWM,set}$ is 64 × T_{SW}. Therefore, in the steady state, T_{PWM} is regulated around 64 × T_{SW}. When light-to-heavy load transient happens, as shown in Fig. 12(a), the TX requires a longer on time (T_{ON}) to charge up V_{OUT}. In the next PWM period, a distinct T_{OFF} will be calculated to accommodate the new on/off duty. Given that the transient can happen at any moment in a PWM period, the TX may also need another calculation to accurately track the new load condition at full scale. Benefiting from the non-linear digital-PWM algorithm, the system can achieve an up to 2 × T_{PWM} transient recovery within tens of microseconds, instead of several milliseconds using an analog loop [10]. A similar fashion applies to heavy-to-light load transients, as shown in Fig. 12(b).

Based on (1), the TX needs calculations to find the next T_{OFF}. Compared to digital multipliers, using a lookup table (LUT) is a more efficient solution, given that T_{OFF} is limited in (0, 64). However, an LUT covering all T_{OFF}–T_{PWM} combinations still requires a large memory occupying an impractical silicon area. To solve this, a coarse-fine searching technique is proposed, as shown in Fig. 13. In the coarse loop, T_{OFF} and T_{PWM} are counted by every 8 × T_{SW}, both of which are then mapped in an LUT. Hence, the LUT size can be reduced by 64×. If the coarse loop returns the same results for two

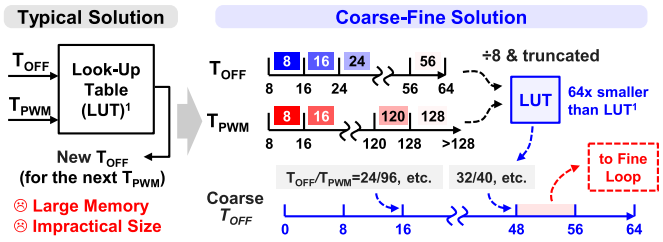

Fig. 13. Proposed coarse-fine searching technique in the global digital-PWM controller.

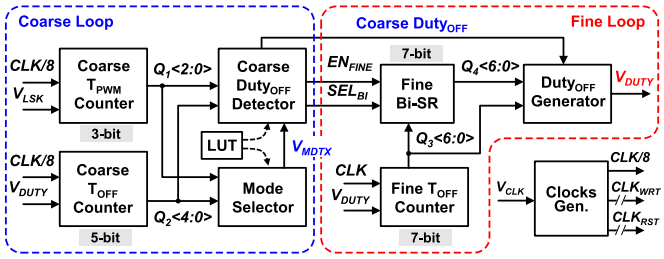

Fig. 14. Global digital-PWM controller at TX.

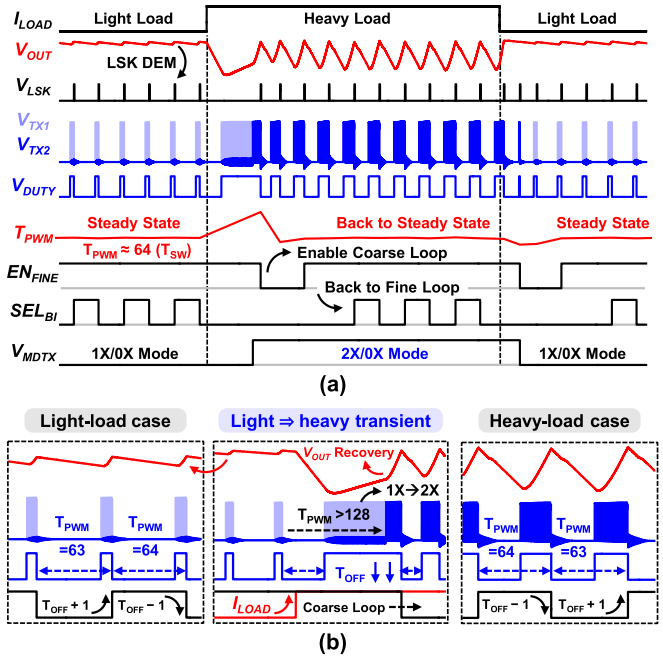

Fig. 15. Operation waveform of the global digital-PWM controller at TX. (a) Load-transient waveform. (b) Zoomed-in waveform.

consecutive T_{PWM}, the TX will switch to the fine loop, where the T_{OFF} will be incrementally adjusted by every single T_{SW} till T_{PWM} equals 64 × T_{SW}.

Fig. 14 shows the circuit implementation of the proposed global digital-PWM controller, with the operation waveform depicted in Fig. 15. Besides T_{OFF}, the coarse loop also determines the active mode of TX. To optimize the tradeoff between output power and power efficiency, the 2X-mode of TX is activated only when the 1X-mode TX cannot supply sufficient power. This is detected by two conditions: 1) T_{OFF} equals 1 × T_{SW} with 1X-mode TX and 2) counted T_{PWM} exceeds 128 × T_{SW}. Condition 1) addresses steadily heavy-load cases. When

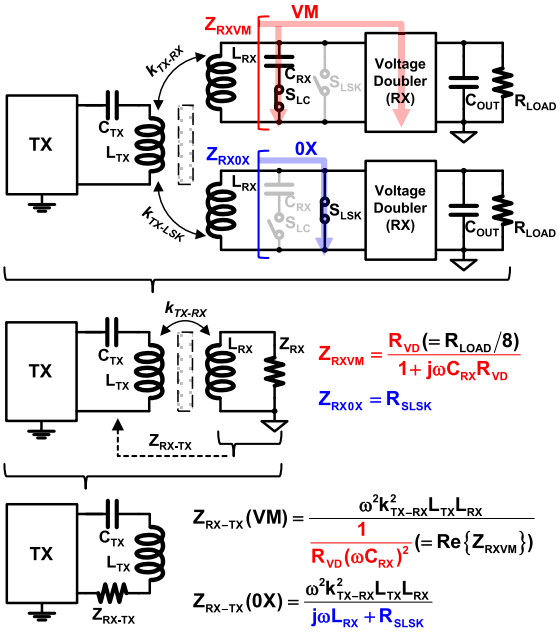

Fig. 16. Principle of the in-band LSK-based RX-to-TX data transfer in the proposed system.

the TX switches to 2X mode under condition 1), T_{OFF} is set to 8 × T_{SW}. Condition 2) handles unpredictable load transients, performing immediate 1X-to-2X mode transition without waiting for the end of the PWM period. The TX 2X-to-1X mode transition occurs when T_{OFF} exceeds 56 × T_{SW} in 2X mode, ensuring that the concurrent load condition can be easily handled by the 1X mode. When TX backs to the 1X mode, T_{OFF} is set to 32 × T_{SW}. A power overlap should be applied between the prior 2X mode and the next 1X mode operation to avoid mode jumping back. Besides both loops, a logic clock generator, derived from the 13.56-MHz system clock V_{CLK}, is applied, generating distributed clock signals for blocks to prevent race hazard issues.

C. Voltage-Sensing LSK Demodulator

The data transfer between RX and TX is essential to achieve global power control. Traditionally, this is accomplished through wireless communication techniques such as Bluetooth or a dedicated data transfer link [34]. Since these solutions inevitably increase system cost and volume, in-band techniques have been recently developed to transfer data directly through the power link [35], [36], [37]. For RX-to-TX data transfer, LSK and frequency-shift-keying (FSK) are two appealing options [13]. However, many biomedical WPT systems require a fixed switching frequency to reduce electromagnetic interference (EMI) in adjacent signal processing units, making LSK the only viable solution. Fig. 16 shows the principle of the LSK-based RX-to-TX data transfer in the proposed system. By changing the equivalent impedance of RX, Z_{RX}, the impedance difference will be reflected to the TX, resulting in a loop current/voltage change at TX. When RX works in VM, Z_{RXVM} is regarded as the C_{RX} in-parallel connected with the VD. The input impedance of the VD can be approximated as (R_{LOAD}/8) [38]. In contrast, Z_{RX0X} equals

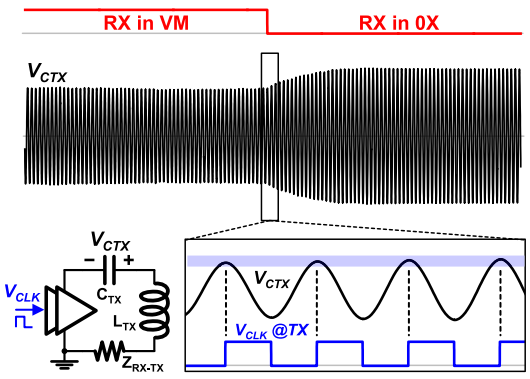

Fig. 17. Operation principle of the voltage-sensing LSK demodulation at TX.

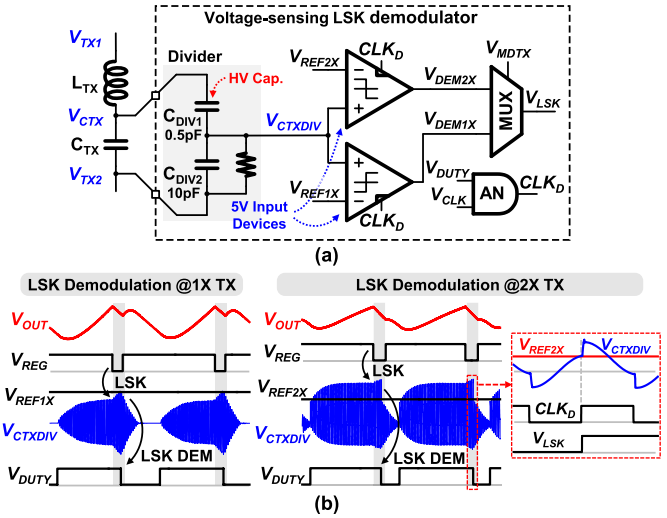

Fig. 18. Voltage-sensing LSK demodulator at TX. (a) Implementation. (b) Operation waveform.

R_{SLSK} when Rx is in the 0X phase. The reflected equivalent impedance of RX at the TX side, $Z_{RX\text{-}TX}$, can be expressed as follows [13]:

$$Z_{RX\text{-}TX} = \frac{\omega^2 k_{TX\text{-}RX}^2 L_{TX} L_{RX}}{j\omega L_{RX} + R_{LRX} + Z_{RX}} \tag{2}$$

where $k_{TX\text{-}RX}$ is the L_{TX}–L_{RX} coupling coefficient and R_{LRX} is the internal resistance of L_{RX}. The $Z_{RX\text{-}TX}$ expressions in different modes are shown in Fig. 16.

Conventionally, the in-band LSK demodulation is performed using an off-chip sensing coil or an on-chip current sensor to detect the changes in the L_{TX}–C_{TX} loop current at TX. This work proposes an LSK demodulation method that senses the voltage on C_{TX} (V_{CTX}), as shown in Fig. 17. Given that L_{TX} and C_{TX} resonate at the switching frequency, the rising edge of V_{CLK} aligns with the positive peak of V_{CTX}. Hence, the TX simply utilizes a clocked comparator to detect the amplitude changes in V_{CTX}, eliminating the need for envelope detectors and continuous-time amplifiers in conventional solutions. Fig. 18 illustrates the implementation of the proposed LSK demodulator. To ensure safe voltage detection, V_{CTX} is divided using an on-chip capacitive divider. Considering that V_{CTX} can reach amplitudes of tens of volts, C_{DIV1} and C_{DIV2} were implemented using high-voltage metal–oxide–metal capacitors.

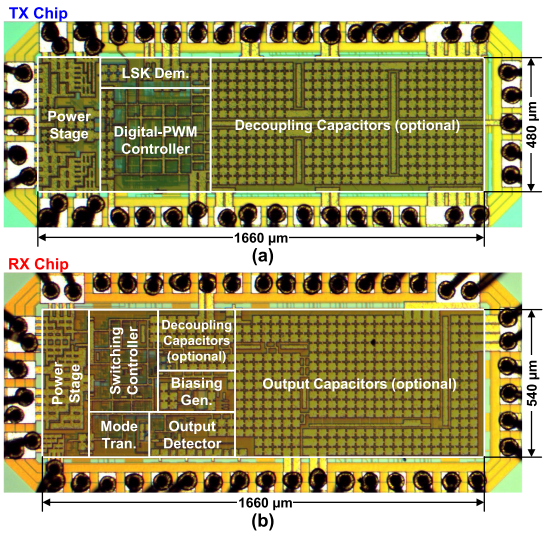

Fig. 19. Chip micrograph. (a) TX chip. (b) RX chip.

In addition, the input pairs of the post comparators were designed with 5 V MOSFETs instead of 1.8-V ones, providing sufficient margin for V_{CTXDIV} swing. The distorted V_{CTXDIV} waveform in 2X-mode TX, caused by the level shift of V_{TX2}, will not affect the amplitude detection because V_{TX2} is at the ground during the V_{CLK} (also CLK_D) rising edge.

IV. Experimental Results

The prototype TX and RX chips were fabricated in a 180-nm CMOS process, mostly using 1.8-V MOSFET devices. As shown in Fig. 19, the TX and RX chips occupy 0.8- and 0.9-mm^2 silicon area, respectively, excluding pads. Both chip areas are dominated by input and output decoupling capacitors, which can be removed if off-chip capacitors are closely used. In the experimental measurement setup, as shown in Fig. 20, off-chip buffer capacitors of 330 nF were added for each of C_{O1} and C_{O2} at RX, which are not necessary for light loads but ensures the heavy-load ability. The TX chip is powered by a 1.8-V dc supply. Measured by an impedance analyzer, the PCB coil L_{TX} has an inductance of 1.39 μH at 13.56 MHz with a 30-mm outer diameter, while L_{RX} is 295 nH with a 20-mm outer diameter. Both single-layer coils have a 0.7-mm trace width and 60-μm copper thickness. C_{TX} and C_{RX} have the capacitance of 100 and 470 pF, respectively. The coil distance between L_{TX} and L_{RX} can be adjusted to mimic the varying coupling conditions in real-world applications.

Fig. 21 shows the measured steady-state operation when the coil distance is 1.25 cm, and the load current, I_{LOAD}, is 30 mA. In this strong-coupling and heavy-load condition, the RX switches its operation between VM and 0X, regulating V_{OUT} at 1.8 V with the help of the global PWM control. The measured V_{OUT} exhibits a ripple of 100 mV. The TX operates in 2X/0X mode to accommodate the heavy load. Through global PWM control, T_{PWM} is stabilized at 64 $\times$ T_{SW}, with a constant on/off duty ratio. With the same coil distance, Fig. 22 shows the measured steady state when I_{LOAD} decreases to 1.8 mA. Due to this light load, V_{OUT} can increase after turning off the TX by harvesting the residual energy in the L_{TX}–C_{TX}

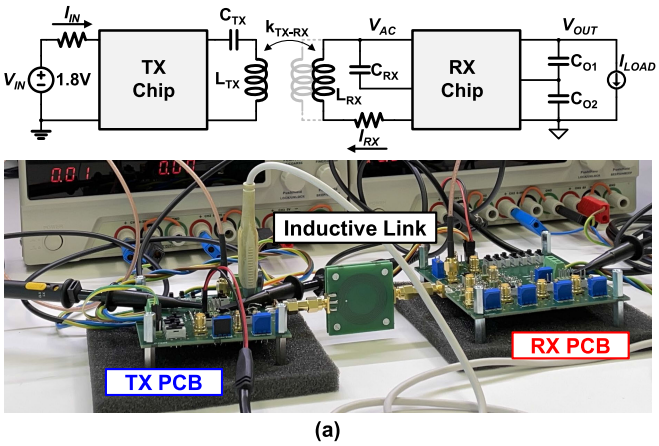

Link Information (measured by impedance analyzer Keysight E4990A)			
L_{TX}	1.39μH	L_{RX}	295nH
Q_{LTX}	155.2	Q_{LRX}	108.3

Fig. 20. Measurement setup. (a) Testbench schematic and photograph. (b) Inductive link information.

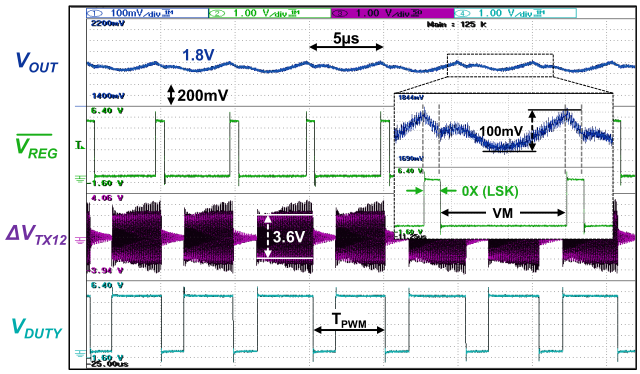

Fig. 21. Measured steady-state operation with 30-mA I_{LOAD} at 1.25-cm coil distance.

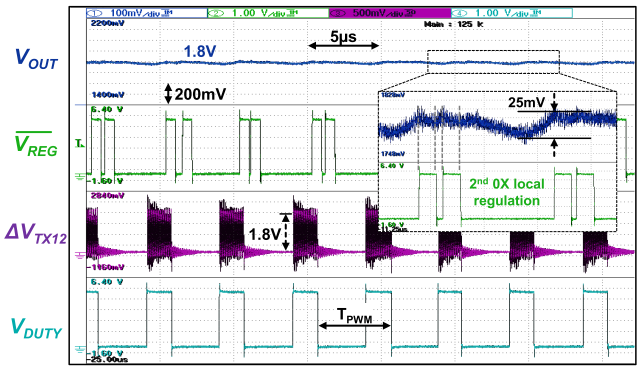

Fig. 22. Measured steady-state operation with 1.8-mA I_{LOAD} at 1.25-cm coil distance.

tank. Hence, it is observed that the RX uses a second 0X pulse to achieve local V_{OUT} regulation. In this state, V_{OUT} shows a 25-mV ripple, while the TX operates in 1X/0X mode.

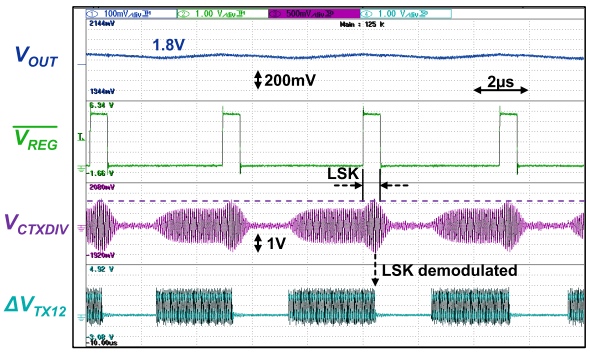

Fig. 23. Measured LSK-based RX-to-TX data transfer with the proposed voltage-sensing LSK demodulation.

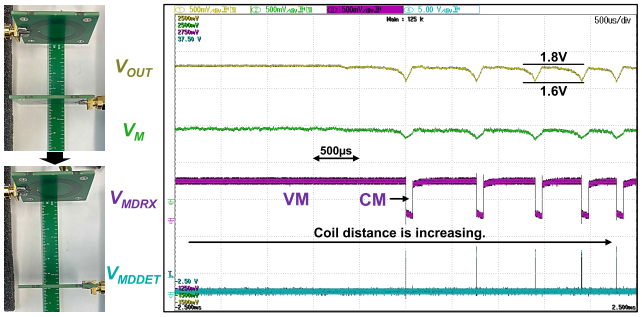

Fig. 24. Measured coupling-transient response with an increasing coil distance with the proposed V/CM RX.

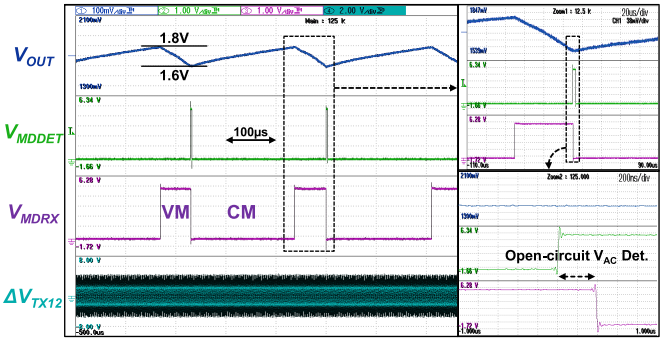

Fig. 25. Measured steady-state operation with 0.5-mA I_{LOAD} at 5.5-cm coil distance.

Fig. 23 illuminates the LSK modem process for RX-to-TX data transfer in the proposed WPT system. It is observed that V_{CTXDIV} presents a clear amplitude increase when the RX enters the 0X phase. By detecting the amplitude increase using the proposed voltage-sensing LSK demodulator, the RX data are recovered at TX, facilitating global power control.

Fig. 24 exhibits the measured coupling-transient response as the coil distance increases when TX continuously operates in 2X mode. It is observed that by moving apart the TX and RX coils, it becomes increasingly challenging for VM operation to regulate V_{OUT} at 1.8 V. To compensate, CM operation is engaged more frequently to stabilize and recover V_{OUT}. Fig. 25 illustrates the measured steady-state operation when the coil distance is increased to 5.5 cm. Given the weak-coupling condition, the RX cannot maintain V_{OUT} at 1.8 V through the VM operation. When V_{OUT} drops below 1.6 V, V_{MDDET}

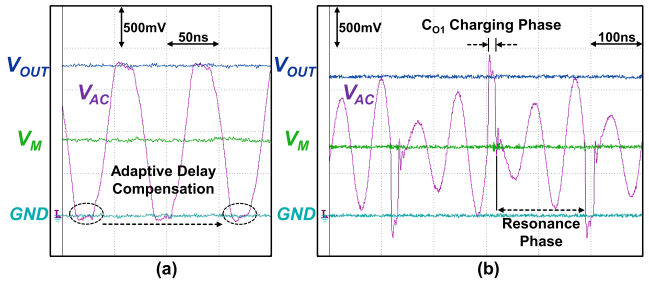

Fig. 26. Measured zoomed-in RX operation waveform. (a) VM operation. (b) Resonant CM operation.

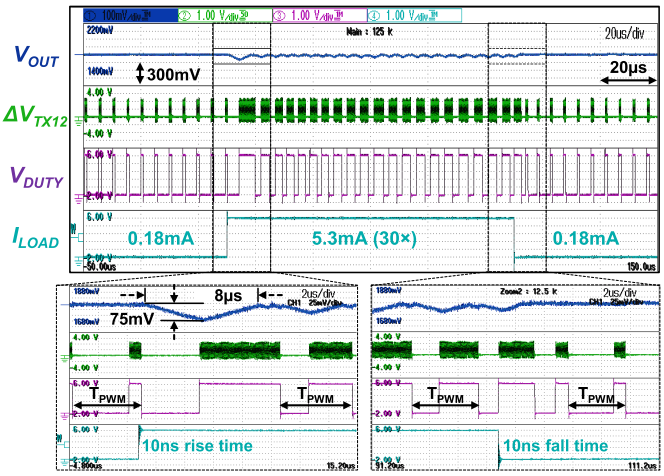

Fig. 27. Measured load-transient operation with I_{LOAD} between 0.18 and 5.3 mA at 0.5-cm coil distance.

goes high to enable the VM-to-CM transition detection, and the RX switches to CM after detecting the open-circuit V_{AC}. It is observed that V_{OUT} is recovered during the CM operation. In this steady state, the RX alternates between VM and CM, regulating V_{OUT} in a 200-mV hysteretic window. Once the coupling condition strengthens sufficiently for the VM RX to charge up V_{OUT}, the RX will not go back to CM, and the global power control will be resumed.

The measured zoomed-in operation waveform at RX is depicted in Fig. 26. The VM operation is shown in Fig. 26(a), where the RX operates as a full-wave VD. It is observed that adaptive delay compensation adjusts the turn-on/-off moment of M_P and M_N, achieving zero-voltage switching (ZVS). In the CM operation shown in Fig. 26(b), the energy accumulation behavior is observable during the resonance phase, given an increasingly larger V_{AC} amplitude. The charging phases for C_{O1} and C_{O2} happen alternately. Benefiting from the adaptive delay compensation, it is observed that ZVS is achieved at both the start and end moments of the charging phases.

The load-transient operation was measured when I_{LOAD} changes between 0.18 and 5.3 mA, with a 10-ns rise/fall time and a coil distance of 0.5 cm. The waveform is shown in Fig. 27. During the light-to-heavy transient, a 75-mV undershoot is observed, and V_{OUT} is recovered within 8 μs. Once the transient T_{PWM} is over, the digital-PWM controller at TX calculates its on/off duty ratio and generates a new T_{OFF} in the next T_{PWM}, as verified in Fig. 27. Thus, the system backs to the steady state after the 8-μs recovery time, showing

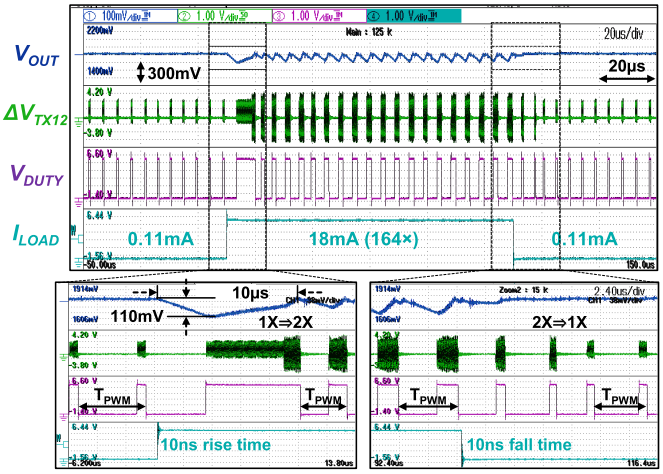

Fig. 28. Measured load-transient operation with I_{LOAD} between 0.11 and 18 mA at 0.5-cm coil distance.

a fast transient response. During the heavy-to-light transient, no overshoot is observed, thanks to the instant LSK-based RX-to-TX communication and the RX local V_{OUT} regulation, and the system backs to the steady state in 2 × T_{PWM}.

Fig. 28 shows the measured load-transient operation when I_{LOAD} changes between 0.11 and 18 mA. During the light-to-heavy transient, V_{OUT} depicts a 110-mV undershoot, which is then recovered within 10 μs. To accommodate the resulting 18-mA heavy load, the TX switches from 1X/0X to 2X/0X operation. The heavy-to-light transient happens with unnoticeable overshoots, and the TX reverts to 1X/0X operation afterward, catering to the light load. Fast transient recovery is also observable during this load transient, thanks to the digital-PWM control strategy.

By integrating the CM operation at RX, the system survives in weaker coupling conditions with longer coil distances between L_{TX} and L_{RX}, namely, the WPT range. The measured results are shown in Fig. 29. With the 1X-mode TX, it is observed that the proposed V/CM RX achieves 1.5× wider WPT range compared to the VM operation at I_{LOAD} of 0.18 mA. The widest WPT range reaches 6 cm when the TX operates in 1X/0X-mode. Furthermore, employing the 2X/0X-mode TX extends the WPT range to 7 cm at the same I_{LOAD}, showing a 1.4× extension compared to VM operation. Fig. 29(c) shows the relationship between the maximum operable coil distance and I_{LOAD} for various operational configurations. It is observed that the V/CM RX significantly improves V_{OUT} regulation at 1.8 V compared to merely increasing the TX power from 1X to 2X mode. By utilizing both V/CM RX and 2X-mode TX, the maximum operable coil distance is further extended beyond the baseline performance achieved with 1X-mode TX and VM-only RX. The system attains its widest WPT range of 7.2 cm at I_{LOAD} of 0.1 mA.

The power efficiency was measured at $V_{IN} = V_{OUT} = 1.8$ V, as shown in Fig. 30(a)–(e). Fig. 30(a) shows the measured E2E efficiency at 0.5-cm coil distance utilizing different regulation methods. It is observed that the peak E2E efficiency of the proposed system achieves 72.3% at $I_{LOAD} = 12$ mA, with TX

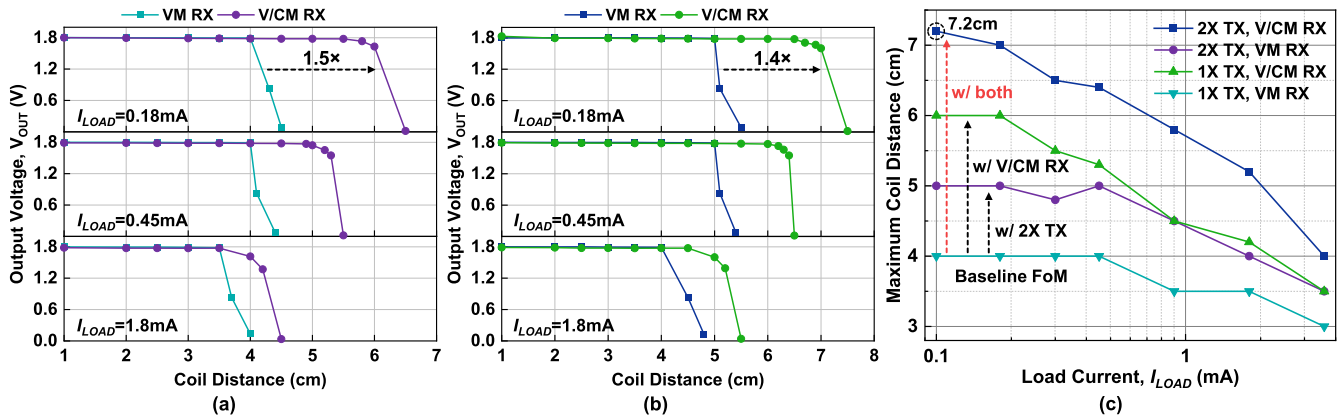

Fig. 29. Measured WPT range in different I_{LOAD} conditions. (a) With 1X-mode TX. (b) With 2X-mode TX. (c) Measured maximum coil distance versus I_{LOAD}.

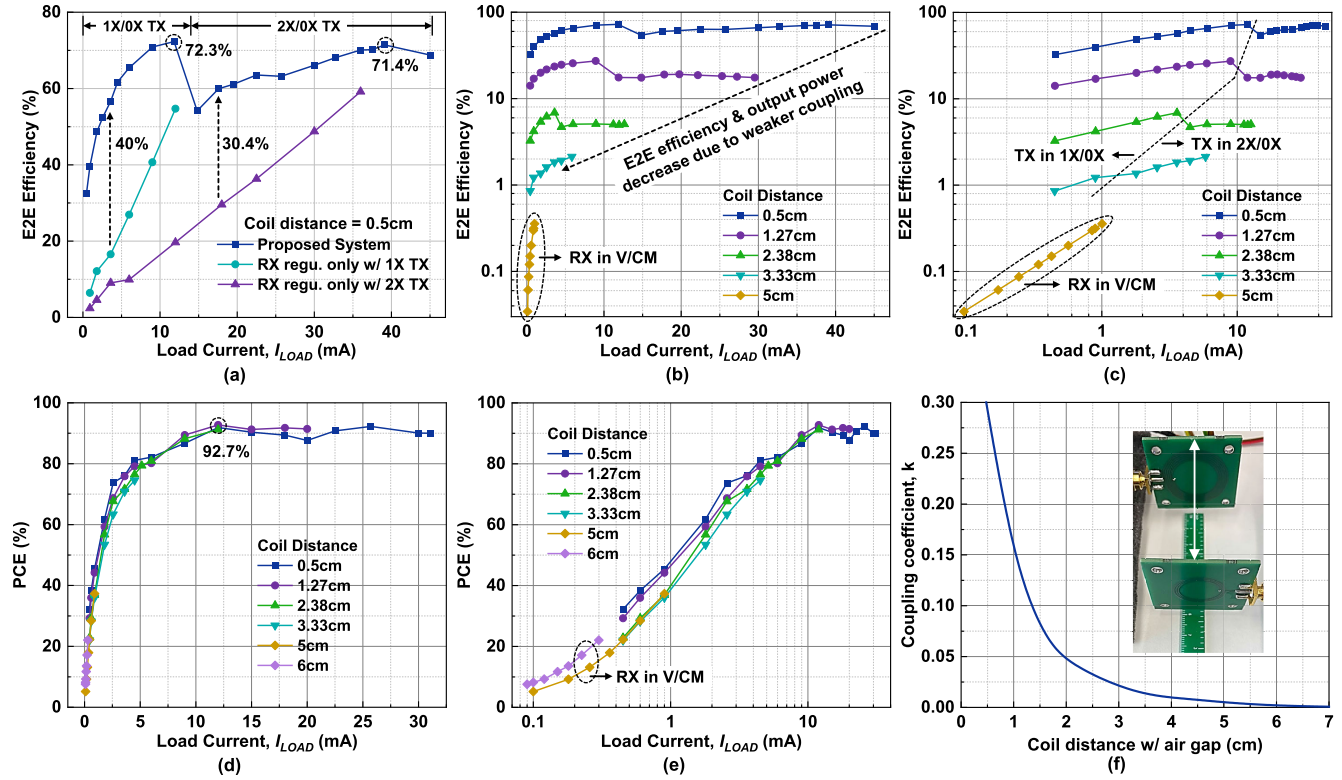

Fig. 30. Measured power efficiency. (a) E2E efficiency versus I_{LOAD} with different regulation methods. (b) and (c) E2E efficiency versus I_{LOAD} under different coupling conditions. (d) and (e) PCE versus I_{LOAD} at RX under different coupling conditions. (f) Measured coupling coefficient versus coil distance with air gap.

in 1X/0X mode. When the TX operates in 2X/0X mode, the E2E efficiency reaches the peak of 71.4% at $I_{\mathrm{LOAD}} = 39$ mA. With the global PWM power regulation, up to 40.5% and 30.4% enhancements in E2E efficiency are achieved compared to the scenarios where the output regulation solely relies on RX while the TX stays operating in the 1X- and 2X-only modes, respectively. The maximum output power is achieved at 81 mW. Fig. 30(b) and (c) shows the measured E2E efficiency at various coil distances. The E2E efficiency is the product of the TX efficiency, the wireless link efficiency [or power transfer efficiency (PTE)], and the PCE at RX. As the coil distance increases, the link efficiency decreases, leading to both reduced E2E efficiency and lower output power. When the coil distance reaches 5 cm, the V/CM operation takes over at RX, accommodating the low input power at RX. Moreover, Fig. 30(d) and (e) presents the measured PCE at RX. The peak PCE of 92.7% is obtained when I_{LOAD} is 12 mA at 1.27-cm coil distance. When the distance is set to 5 and 6 cm, the RX operates in V/CM. Fig. 30(f) shows the measured coupling coefficient versus coil distance using an impedance analyzer.

Table I benchmarks this work among recently reported WPT systems. The proposed WPT system achieves a wide WPT range, improving the weak-coupling performance. It also realizes high E2E efficiency, fast load-transient recovery, small

TABLE I
COMPARISONS WITH STATE-OF-THE-ART DESIGNS

	TBCAS' 15 [7]	JSSC' 18 [8]	JSSC' 21 [9]	JSSC' 22 [11]	TBCAS' 22 [10]	JSSC' 23 [12]	This Work
Technology	350nm CMOS	65nm CMOS	250nm CMOS	180nm CMOS	180nm CMOS	180nm CMOS	**180nm CMOS**
WPT Architecture	Series-Parallel	Series-Parallel	Series-Series	Series-Parallel	Series-Parallel	Series-Series	**Series-Parallel**
TX Topology	Buck + Class-D	Class-D	Diff. Class-D	Class-D	3-Mode Class-D	Diff. Class-D	**3-Mode Class-D**
RX Topology	1X/2X FBR	FBR	FBR	FBR	FBR	FBR	**V/CM VD**
Frequency (MHz)	13.56	13.56	6.78	6.78	13.56	6.78	**13.56**
Coil Diameter (cm)	TX 5; RX 1	TX 3.5; RX 2	TX 4.5; RX 4.5	TX 3.2; RX 2.5	TX 4; RX 2.2	TX 5; RX 5	**TX 3; RX 2**
Off-Chip Components (exclude WPT link)	1 coil, 2 C_{OUT}, 1 global controller	1 coil, 1 C_{OUT}	1 coil, 1 C_{OUT}, 1 data demodulator	1 C_{OUT} (8μF)	1 coil, 1 C_{OUT} (2.2μF)	1 C_{OUT} (10μF)	**2 C_{OUT} (330nF each)**
Global Regulation Method	Supply modulation	Constant off-time	PWM (CCM)	Hysteretic	PWM (DCM)	PWM (CCM)	**Digital-PWM (DCM)**
Global Data Link (Fully integrated ?)	Wireless LSK (No)	Wireless LSK (No)	Wireless LSK (No)	Wireless LSK (Yes)	Wireless LSK (No)	Wireless Phase Shift (Yes)	**Wireless LSK (Yes)**
Data Demodulation @TX (Implementation)	I_{TX} Sensing (3^{rd} coil)	I_{TX} Sensing (3^{rd} coil)	I_{TX} Sensing (3^{rd} coil)	I_{TX} Sensing (Current Sensor)	I_{TX} Sensing (3^{rd} coil)	Phase Shift Detector	**V_{CTX} Sensing (Comparator)**
V_{IN} @TX / V_{OUT} @RX (V)	(N/R) / 3.7	2.5 / (1.2-2.5)	5 / 5	1.8 / (1.1-1.8)	(N/R) / 3.3	3.3 / 3.3	**1.8 / 1.8**
V_{OUT} ripple (mV) @I_{LOAD}	N/R	100 @10mA	200 @50mA	75 (Hysteretic)	100 @16.5mA	N/R	**25 @ 1.8mA; 100 @30mA**
Max. Output Power (mW) (@D_{coil})	234 (@0.3cm)	49.4 (@0.6cm)	400 (@0.3cm)	63 (@0.65cm)	162 (@0.3cm)	900 (@2cm)	**81 (@0.5cm)**
Load Tran. Recovery (μs) (@Step Ratio)	2000 (@1:10)	0 (@1:10)	820 (@1:3)	0 (@1:3)	1100 (@1:10)	70 (@1:4)	**10 (@1:164)**
Max. WPT Range (cm) (@I_{LOAD})	1.8 (@13.5mA)	1.15 (@4mA)	0.3 (@50mA)	1.15 (@22mA)	1 (@21mA)	2 (@273mA)	**7.2 (@0.1mA); 5.2 (@1.8mA)**
Peak E2E Efficiency (@D_{coil})	62.4% (@0.3cm)	70.6% (@0.6cm)	71.5% (@0.3cm)	68.9% (@0.7cm)	70.1% (@0.1cm)	77% (@1.5cm)	**72.3% @1X TX; 71.4% @2X TX (@0.5cm)**

N/R: not reported; CCM: continuous conduction mode; DCM: discontinuous conduction mode.

output voltage ripple with nanofarad buffer capacitors, and a high level of integration.

V. CONCLUSION

This article presents a 13.56-MHz coupling-adaptive WPT system for biomedical implantable applications. Thanks to the hybrid V/CM RX, the proposed system achieves a WPT range of up to 7.2 cm, extending by up to 1.5× compared to conventional VM-only operations. With the help of the global digital-PWM control, the system attains up to 72.3% E2E efficiency and fast load-transient recovery within 10 μs. Benefiting from the adaptive delay compensated switching control, up to 92.7% PCE is obtained at RX. In addition, this work introduces a fully integrated voltage-sensing LSK demodulator, offering simplified circuit implementations and reduced power consumption than current-sensing methods. With the TX powered by a 1.8-V dc supply, the proposed WPT system delivers a regulated 1.8-V dc output at RX, with a maximum output power of 81 mW.

REFERENCES

[1] M. Kiani, "Wireless power transfer and management for medical applications: Wireless power," *IEEE Solid StateCircuits Mag.*, vol. 14, no. 3, pp. 41–52, Jul. 2022.

[2] A. Finn, D. Grewal, and L. Vajzovic, "Argus II retinal prosthesis system: A review of patient selection criteria, surgical considerations, and post-operative outcomes," *Clin. Ophthalmology*, vol. 12, pp. 1089–1097, Jun. 2018.

[3] Y. Jia et al., "A trimodal wireless implantable neural interface system-on-chip," *IEEE Trans. Biomed. Circuits Syst.*, vol. 14, no. 6, pp. 1207–1217, Dec. 2020.

[4] Y. Park et al., "A wireless power and data transfer IC for neural prostheses using a single inductive link with frequency-splitting characteristic," *IEEE Trans. Biomed. Circuits Syst.*, vol. 15, no. 6, pp. 1306–1319, Dec. 2021.

[5] Y. Lu and W.-H. Ki, "A 13.56 MHz CMOS active rectifier with switched-offset and compensated biasing for biomedical wireless power transfer systems," *IEEE Trans. Biomed. Circuits Syst.*, vol. 8, no. 3, pp. 334–344, Jun. 2014.

[6] Y. Lu, M. Huang, L. Cheng, W.-H. Ki, U. Seng-Pan, and R. P. Martins, "A dual-output wireless power transfer system with active rectifier and three-level operation," *IEEE Trans. Power Electron.*, vol. 32, no. 2, pp. 927–930, Feb. 2017.

[7] X. Li, X. Meng, C.-Y. Tsui, and W.-H. Ki, "Reconfigurable resonant regulating rectifier with primary equalization for extended coupling- and loading-range in bio-implant wireless power transfer," *IEEE Trans. Biomed. Circuits Syst.*, vol. 9, no. 6, pp. 875–884, Dec. 2015.

[8] C. Huang, T. Kawajiri, and H. Ishikuro, "A 13.56-MHz wireless power transfer system with enhanced load-transient response and efficiency by fully integrated wireless constant-idle-time control for biomedical implants," *IEEE J. Solid-State Circuits*, vol. 53, no. 2, pp. 538–551, Feb. 2018.

[9] F.-B. Yang, J. Fuh, Y.-H. Li, M. Takamiya, and P.-H. Chen, "Structure-reconfigurable power amplifier (SR-PA) and 0X/1X regulating rectifier for adaptive power control in wireless power transfer system," *IEEE J. Solid-State Circuits*, vol. 56, no. 7, pp. 2054–2064, Jul. 2021.

[10] G. Namgoong, W. Park, and F. Bien, "A 13.56 MHz wireless power transfer system with fully integrated PLL-based frequency-regulated reconfigurable duty control for implantable medical devices," *IEEE Trans. Biomed. Circuits Syst.*, vol. 16, no. 6, pp. 1116–1128, Dec. 2022.

[11] J. Tang, L. Zhao, and C. Huang, "A wireless hysteretic controlled wireless power transfer system with enhanced efficiency and dynamic response for bioimplants," *IEEE J. Solid-State Circuits*, vol. 58, no. 4, pp. 1160–1171, Apr. 2023.

[12] X. Bai, Y. Lu, C. Zhan, and R. P. Martins, "A 6.78-MHz wireless power transfer system with inherent wireless phase shift control without feedback data sensing coil," *IEEE J. Solid-State Circuits*, vol. 58, no. 6, pp. 1746–1757, Jun. 2023.

[13] M. G. P. Perez-Nicoli and F. Silveira, *Inductive Links for Wireless Power Transfer: Fundamental Concepts for Designing High-efficiency Wireless Power Transfer Links*. Cham, Switzerland: Springer, 2021.

[14] T. Lu and S. Du, "27.4 A 13.56MHz wireless power transfer system with hybrid voltage-/current-mode receiver and global digital-PWM regulation achieving 150% transfer range extension and 72.3% end-to-end efficiency," in *Proc. IEEE Int. Solid-State Circuits Conf. (ISSCC)*, vol. 67, Feb. 2024, pp. 450–452.

[15] L. Cheng, W.-H. Ki, and C.-Y. Tsui, "A 6.78-MHz single-stage wireless power receiver using a 3-mode reconfigurable resonant regulating rectifier," *IEEE J. Solid-State Circuits*, vol. 52, no. 5, pp. 1412–1423, May 2017.

[16] J. Lin, Y. Lu, C. Zhan, and R. P. Martins, "A single-stage dual-output regulating rectifier with hysteretic current-wave modulation," *IEEE J. Solid-State Circuits*, vol. 56, no. 9, pp. 2770–2780, Sep. 2021.

[17] S. Liu et al., "A single-stage three-mode reconfigurable regulating rectifier for wireless power transfer," *IEEE Trans. Power Electron.*, vol. 38, no. 7, pp. 9195–9205, Jul. 2023.

[18] Z. Luo, J. Liu, and H. Lee, "A high-efficiency 40.68-MHz single-stage dual-output regulating rectifier with ZVS and synchronous PFM control for wireless powering," *IEEE J. Solid-State Circuits*, vol. 59, no. 8, pp. 2418–2429, Aug. 2024.

[19] H.-S. Lee, K. Eom, and H.-M. Lee, "27.3 A 90.8%-efficiency SIMO resonant regulating rectifier generating 3 outputs in a half cycle with distributed multi-phase control for wirelessly-powered implantable devices," in *Proc. IEEE Int. Solid-State Circuits Conf. (ISSCC)*, vol. 67, Feb. 2024, pp. 448–450.

[20] T. Lu and S. Du, "A single-stage regulating voltage-doubling rectifier for wireless power transfer," *IEEE Solid-State Circuits Lett.*, vol. 6, pp. 29–32, 2023.

[21] T. Lu, Z.-Y. Chang, J. Jiang, K. Makinwa, and S. Du, "A 13.56MHz fully integrated 91.8% efficiency single-stage dual-output regulating voltage doubler for biomedical wireless power transfer," in *Proc. IEEE Custom Integr. Circuits Conf. (CICC)*, Apr. 2023, pp. 1–2.

[22] T. Lu, K. A. A. Makinwa, and S. Du, "A single-stage dual-output regulating voltage doubler for wireless power transfer," *IEEE J. Solid-State Circuits*, vol. 59, no. 9, pp. 2922–2933, Sep. 2024.

[23] M. Choi, T. Jang, J. Jeong, S. Jeong, D. Blaauw, and D. Sylvester, "A resonant current-mode wireless power receiver and battery charger with -32 dBm sensitivity for implantable systems," *IEEE J. Solid-State Circuits*, vol. 51, no. 12, pp. 2880–2892, Dec. 2016.

[24] H.-S. Lee et al., "A power-efficient resonant current mode receiver with wide input range over breakdown voltages using automated maximum efficiency control," *IEEE Trans. Power Electron.*, vol. 37, no. 7, pp. 8738–8750, Jul. 2022.

[25] H. S. Gougheri and M. Kiani, "Self-regulated reconfigurable voltage/current-mode inductive power management," *IEEE J. Solid-State Circuits*, vol. 52, no. 11, pp. 3056–3070, Nov. 2017.

[26] H. Sadeghi Gougheri and M. Kiani, "An inductive voltage-/current-mode integrated power management with seamless mode transition and energy recycling," *IEEE J. Solid-State Circuits*, vol. 54, no. 3, pp. 874–884, Mar. 2019.

[27] F. Mao, R. Martins, and Y. Lu, "27.1 A differential hybrid class-ED power amplifier with 27W maximum power and 82% peak E2E efficiency for wireless fast charging to-go," in *Proc. IEEE Int. Solid-State Circuits Conf. (ISSCC)*, vol. 67, Feb. 2024, pp. 444–446.

[28] Y. Lu and W.-H. Ki, *CMOS Integrated Circuit Design for Wireless Power Transfer*. Cham, Switzerland: Springer, 2018.

[29] X. Ge, L. Cheng, Y. Yao, and W.-H. Ki, "A 6.78 MHz single-stage wireless power transmitter using a 3-mode zero-voltage switching class-D PA," *IEEE Trans. Circuits Syst. I, Reg. Papers*, vol. 68, no. 6, pp. 2736–2748, Jun. 2021.

[30] Y. Chen, Y. Luo, and J. Guo, "A 1-W, 6.78-MHz wireless power transfer system with up-to-16.1% light-load efficiency improvement and instant response through single-cycle-based DTX control," *IEEE Trans. Power Electron.*, vol. 38, no. 2, pp. 2743–2753, Feb. 2023.

[31] J. Tang, L. Zhao, and C. Huang, "A through-power-link hysteretic-controlled capacitive isolated DC–DC converter with enhanced efficiency and common-mode transient immunity," *IEEE J. Solid-State Circuits*, vol. 59, no. 5, pp. 1543–1555, May 2024.

[32] C. Huang, T. Kawajiri, and H. Ishikuro, "A near-optimum 13.56 MHz CMOS active rectifier with circuit-delay real-time calibrations for high-current biomedical implants," *IEEE J. Solid-State Circuits*, vol. 51, no. 8, pp. 1797–1809, Aug. 2016.

[33] L. Cheng, W.-H. Ki, Y. Lu, and T.-S. Yim, "Adaptive on/off delay-compensated active rectifiers for wireless power transfer systems," *IEEE J. Solid-State Circuits*, vol. 51, no. 3, pp. 712–723, Mar. 2016.

[34] B. Lee and M. Ghovanloo, "An overview of data telemetry in inductively powered implantable biomedical devices," *IEEE Commun. Mag.*, vol. 57, no. 2, pp. 74–80, Feb. 2019.

[35] S. Ha, C. Kim, J. Park, S. Joshi, and G. Cauwenberghs, "Energy recycling telemetry IC with simultaneous 11.5 mW power and 6.78 Mb/s backward data delivery over a single 13.56 MHz inductive link," *IEEE J. Solid-State Circuits*, vol. 51, no. 11, pp. 2664–2678, Nov. 2016.

[36] Y. Chen, Y. Luo, Y. Lin, L. Shao, D. Chen, and J. Guo, "27.5 A wireless power transfer system with up-to-27.9% efficiency improvement under coupling coefficient ranging from 0.1 to 0.39 based on phase-shift/time-constant detection and hybrid transmission power control," in *Proc. IEEE Int. Solid-State Circuits Conf. (ISSCC)*, vol. 67, Feb. 2024, pp. 452–454.

[37] J. Ge, Y. Lu, R. Yang, D. Pan, and L. Cheng, "27.2 A 6.78-MHz 79.5%-peak-efficiency wireless power transfer system using a wireless mode-recognition technique and a fully-on/off class-d power amplifier," in *Proc. IEEE Int. Solid-State Circuits Conf. (ISSCC)*, vol. 67, Feb. 2024, pp. 446–448.

[38] X. Li, C.-Y. Tsui, and W.-H. Ki, "Power management analysis of inductively-powered implants with 1X/2X reconfigurable rectifier," *IEEE Trans. Circuits Syst. I, Reg. Papers*, vol. 62, no. 3, pp. 617–624, Mar. 2015.

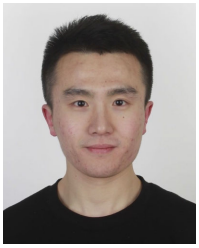

Tianqi Lu (Graduate Student Member, IEEE) received the B.Sc. degree in physics from Nanchang University, Nanchang, China, in 2018, and the M.Sc. degree in integrated circuit engineering from Tsinghua University, Beijing, China, in 2021. He is currently pursuing the Ph.D. degree with the Department of Microelectronics, Delft University of Technology, Delft, The Netherlands.

His research interests include power management integrated circuits for wireless power transfer and dc–dc power converters.

Sijun Du (Senior Member, IEEE) received the B.Eng. degree (Hons.) in electrical engineering from University Pierre and Marie Curie (UPMC), Paris, France, in 2011, the M.Sc. degree (Hons.) in electrical and electronic engineering from the Imperial College, London, U.K., in 2012, and the Ph.D. degree in electrical engineering from the University of Cambridge, Cambridge, U.K., in January 2018.

He worked at the Laboratoire d'Informatique de Paris 6 (LIP6), UPMC, and then was an IC Engineer at Shanghai, China, from 2012 to 2014. He was a Summer Engineer Intern at Qualcomm Technology Inc., San Diego, CA, USA, in 2016. He was a Post-Doctoral Researcher at the Department of Electrical Engineering and Computer Sciences (EECS), University of California at Berkeley, Berkeley, CA, USA, from 2018 to 2020. In 2020, he joined the Department of Microelectronics, Delft University of Technology (TU Delft), Delft, The Netherlands, as an Assistant Professor. His current research is focused on energy-efficient integrated circuits and systems, including power management integrated circuits (PMIC), energy harvesting, wireless power transfer, and dc/dc converters used in Internet-of-Things (IoT) wireless sensors, wearable electronics, and biomedical devices.

Dr. Du has been serving as the IEEE ISSCC Student Research Preview (SRP) Committee Member since 2023. He received the Dutch Research Council (NWO) Talent Program VENI grant in the 2021 round. He was a co-recipient of the Best Student Paper Award from IEEE ICECS 2022. He served as the IEEE ICECS Sub-Committee Chair in 2022 and 2024 and the IEEE ISCAS Sub-Committee Chair in 2025.